Cell Reports

Report

mTORC1 Upregulation Leads to Accumulation of the Oncometabolite Fumarate in a Mouse Model of Renal Cell Carcinoma

Graphical Abstract

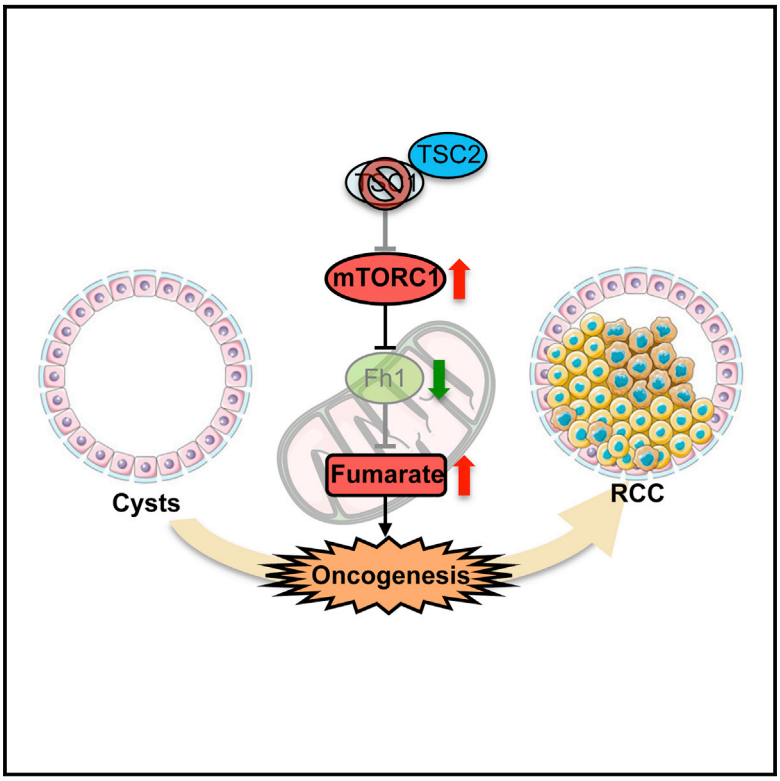

Authors

Luca Drusian, Elisa Agnese Nigro, Valeria Mannella, ..., Giovanna Musco, Christian Frezza, Alessandra Boletta

Correspondence

boletta.alessandra@hsr.it

In Brief

Renal cell carcinomas are common human cancers whose modeling in mice has proved difficult. Drusian et al. show that kidney-specific inactivation of *Tsc1* results in benign lesions that gradually transform into malignant carcinomas. Metabolomic profiling revealed that mTORC1 upregulation leads to accumulation of fumarate, an oncometabolite that contributes to transformation.

Highlights

- A kidney-specific *Tsc1* mutant develops progressive renal cell carcinoma (RCC)
- Several mTORC1-mediated metabolic derangements progressively accumulate in RCC
- Chronic mTORC1 upregulation leads to accumulation of the oncometabolite fumarate
- Fumarate accumulation downstream of mTORC1 contributes to transformation

Drusian et al., 2018, Cell Reports *24*, 1093–1104
July 31, 2018
https://doi.org/10.1016/j.celrep.2018.06.106

CellPress

Cell Reports
Report

mTORC1 Upregulation Leads to Accumulation of the Oncometabolite Fumarate in a Mouse Model of Renal Cell Carcinoma

Luca Drusian,[1,2] Elisa Agnese Nigro,[1] Valeria Mannella,[3] Roberto Pagliarini,[1] Monika Pema,[1] Ana S.H. Costa,[4] Fabio Benigni,[5] Alessandro Larcher,[6] Marco Chiaravalli,[1] Edoardo Gaude,[4] Francesco Montorsi,[5,6] Umberto Capitanio,[5,6] Giovanna Musco,[3] Christian Frezza,[4] and Alessandra Boletta[1,7,*]

[1]Molecular Basis of Cystic Kidney Disorders Unit, Division of Genetics and Cell Biology, IRCCS San Raffaele Scientific Institute, Milan, Italy
[2]PhD Program in Biology and Biotherapy of Cancer, Università Vita-Salute San Raffaele, Milan, Italy
[3]Biomolecular NMR Unit, Division of Genetics and Cell Biology, IRCCS San Raffaele Scientific Institute, Milan, Italy
[4]MRC, Cancer Unit Cambridge, University of Cambridge, Hutchison/MRC Research Centre, Box 197, Cambridge Biomedical Campus, Cambridge, CB2 0XZ, UK
[5]Urological Research Institute (URI), IRCCS San Raffaele Scientific Institute, Milan, Italy
[6]Department of Urology, IRCCS San Raffaele Scientific Institute, Milan, Italy
[7]Lead Contact
*Correspondence: boletta.alessandra@hsr.it
https://doi.org/10.1016/j.celrep.2018.06.106

SUMMARY

Renal cell carcinomas (RCCs) are common cancers diagnosed in more than 350,000 people each year worldwide. Several pathways are de-regulated in RCCs, including mTORC1. However, how mTOR drives tumorigenesis in this context is unknown. The lack of faithful animal models has limited progress in understanding and targeting RCCs. Here, we generated a mouse model harboring the kidney-specific inactivation of *Tsc1*. These animals develop cysts that evolve into papillae, cystadenomas, and papillary carcinomas. Global profiling confirmed several metabolic derangements previously attributed to mTORC1. Notably, *Tsc1* inactivation results in the accumulation of fumarate and in mTOR-dependent downregulation of the TCA cycle enzyme fumarate hydratase (FH). The re-expression of *FH* in cellular systems lacking *Tsc1* partially rescued renal epithelial transformation. Importantly, the mTORC1-FH axis is likely conserved in human RCC specimens. We reveal a role of mTORC1 in renal tumorigenesis, which depends on the oncometabolite fumarate.

INTRODUCTION

Renal cell carcinomas (RCCs) are a group of heterogeneous and common cancers affecting the kidney, with an incidence of 350,000 people newly diagnosed per year (Brugarolas, 2014; Pugh and Ratcliffe, 2003). The most common type of RCC is clear cell RCC (ccRCC), representing approximately 75% of all RCC cases (Chow et al., 2010; Brugarolas, 2014; Capitanio and Montorsi, 2016), followed by papillary RCC (PRCC), which is sub-divided into type I and type II PRCC (Chow et al., 2010; Capitanio and Montorsi, 2016). Type I PRCC is characterized by a chromosome 7 amplification involving the *MET* oncogene, while type II PRCC is most frequently caused by loss of heterozygosity (LOH) of the enzyme fumarate hydratase (*FH*) (Toro et al., 2003), an enzyme of the tricarboxylic acid (TCA) cycle that catalyzes the conversion of fumarate to malate.

The mammalian target of rapamycin (mTOR) pathway plays a central role in RCC oncogenesis and is upregulated in more than 80% of ccRCC cases (Chow et al., 2010; Capitanio and Montorsi, 2016; Brugarolas, 2014), although its role in PRCC has not been investigated to date. The central regulator of the mTOR cascade is the tuberous sclerosis complex (TSC) (Tee et al., 2002), comprising TSC1 (hamartin), TSC2 (tuberin), and TBC1D7 (Dibble et al., 2012). The *TSC1* and *TSC2* genes are mutated in a syndromic form of cancer called the TSC, which also presents with RCC in a small proportion of individuals (2%–3%) (Bjornsson et al., 1996). Among the central functions of mTORC1 is the regulation of cellular metabolism, with glycolysis, the pentose phosphate pathway, and purine and fatty acids biosynthesis all being implicated (Guertin and Sabatini, 2007; Düvel et al., 2010; Menon et al., 2012; Ben-Sahra et al., 2013; Choo et al., 2010; Csibi et al., 2013). However, whether these metabolic changes are secondary effects or actively contribute to tumorigenesis is still unclear.

The lack of animal models that faithfully reproduce the initiation and progression of renal carcinomas has limited progression in the field. Although both *Myc* and *TFEB* overexpression recapitulate some features of RCCs (Shroff et al., 2015; Calcagnì et al., 2016), the inactivation of tumor suppressors, such as *Fh1*, *Vhl*, and *Tsc1*, results in kidney cysts (Frew et al., 2008; Pollard et al., 2007; Onda et al., 1999; Wilson et al., 2005). However, recent studies have demonstrated that the combined inactivation of multiple tumor suppressors results in renal carcinogenesis (Gu et al., 2017; Harlander et al., 2017).

Here, we generated a mouse model in which *Tsc1* is inactivated in a restricted segment of the renal tubule using a kidney-specific Cre (KspCre). These animals developed progressive renal lesions that eventually resulted in cortical renal

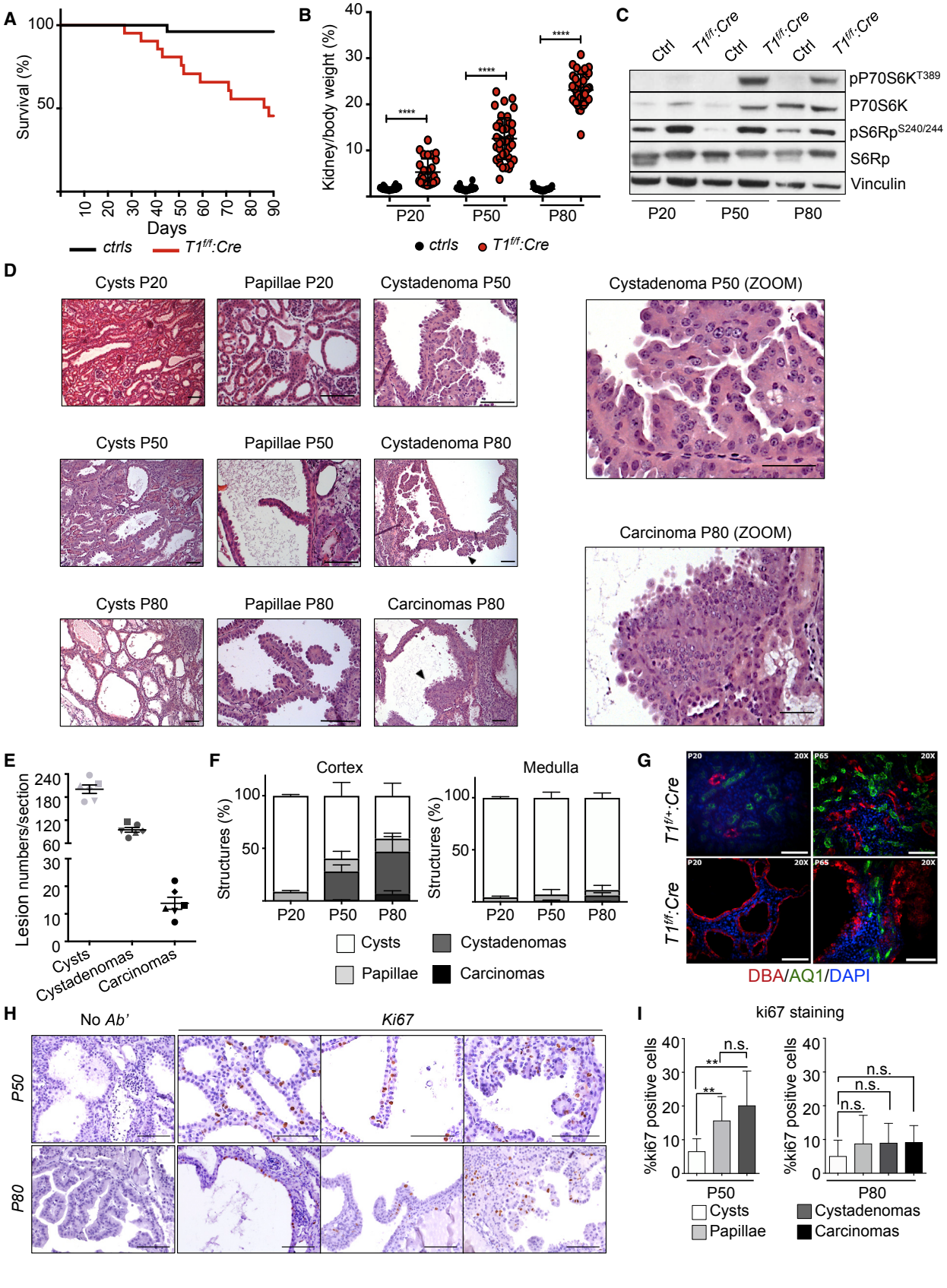

(legend on next page)

papillary carcinomas. Metabolic profiling of the kidneys revealed a regulation by mTORC1 leading to the accumulation of fumarate, a potent oncometabolite that contributes to the cancerous transformation observed in these animals. Importantly, we find a correlation between mTORC1 upregulation and *FH* downregulation in human specimens.

RESULTS AND DISCUSSION

T1$^{f/f}$:Cre Mice as a Model of Progressive Renal Carcinogenesis

To investigate the role of mTORC1 in RCC we crossed animals where the *Tsc1* gene was flanked by lox-p sites (*Tsc1$^{flox/flox}$*) (Kwiatkowski et al., 2002) with animals expressing Cre recombinase in the distal tubules and collecting ducts (KspCre), a Cre line that was not previously used to inactivate *Tsc1* (Shao et al., 2002). *Tsc1$^{flox/flox}$:KspCre* animals, hereafter indicated as *T1$^{f/f}$:Cre*, were born with normal kidneys and manifested a slowly progressive cystic phenotype by P20 (Pema et al., 2016). *T1$^{f/f}$:Cre* mice die within the first 3 months of life, with only 50% of animals surviving up to P80 compared with *T1$^{f/+}$:Cre* (Ctrl) mice (Figure 1A). Mutant mice showed enlarged kidneys, with multiple macroscopic lesions (Figure S1A) and significantly increased kidney/body weight at P20, P50, and P80 (Figure 1B), along with a general reduction in body weight (Figure S1B) and ultimately visible animal sickness at P80. Western blot analysis confirmed the presence of mTORC1 activation at all stages analyzed (Figures 1C and S1C). Histological analysis of mutant *T1$^{f/f}$:Cre* kidneys revealed the presence of cysts with a flat and monolayered epithelium and small papillae in a few cysts (Figures 1D and S1D). At P50, *T1$^{f/f}$:Cre* kidneys presented an increased number of cysts, layered by a cuboidal epithelium (Figures 1D and S1D) along with both "simple" and "complex" papillae layered by a monostratified or multistratified epithelium, respectively. Interestingly, at this stage, the kidneys were characterized by a large number of cystadenomas derived from the wall of the cysts (Figures 1D and S1D). At P80, *T1$^{f/f}$:Cre* kidneys showed increasing numbers of multistratified papillae and cystadenomas as well as a large number of carcinomas (Figures 1D–1F and S1D). Importantly, RCC developed with full penetrance in the totality of the animals analyzed (n = 5). Notably, the cancerous lesions were primarily limited to the renal cortex (Figure 1F). Staining with a distal/collecting duct marker, Dolichos biflorus agglutinin (DBA), showed that at P20, all cysts were positive to DBA, as expected, and at P65, several of the multistratified epithelia were still positive to DBA, indicating that transformation is progressive (Figure 1G). Indeed, staining with Ki67 revealed a progressive increase in proliferation rates in the modified epithelia (Figures 1H and 1I). Thus, the present data show that the inactivation of *Tsc1* in a restricted segment of the kidney results in progressive and robust RCC development, unlike the inactivation using a Cre line with broader expression (Traykova-Brauch et al., 2008).

Metabolomic Profiling of *T1$^{f/f}$:Cre* Kidneys Reveals Fumarate Accumulation

Because mTORC1 plays a key role in the regulation of cellular metabolism, we performed global metabolomics in the *T1$^{f/f}$:Cre* murine renal cancerous lesions. To this end, we used nuclear magnetic resonance (NMR) spectroscopy to analyze the renal cortex of *T1$^{f/f}$:Cre* animals. As control *T1$^{f/+}$:Cre* and *T1$^{+/+}$:Cre* mice (indicated as Ctrls) were used interchangeably, and gender was equally distributed between male and female. Principal-component analysis (PCA) revealed a clear separation between Ctrls and mutant kidneys at both P50 and P80 (Figures 2A, S2A, and S2B). A multivariate supervised statistical analysis (partial least squares discriminant analysis [PLS-DA]) revealed that this separation was due to a total of 50 and 51 spectral bins significantly different at P50 or P80, out of which we were able to assign 32 and 33 metabolites, respectively (Figures S2A and S2B; Table S1). Enrichment pathway analysis revealed that 20 pathways were altered at P50, and 16 pathways were altered at P80 (Figures 2B and 2C; Table S1). As expected, among the pathways that appeared differentially enriched were glutaminolysis, glycolysis, and purine biosynthesis, all previously implicated in the mTORC1 cascade (Figures 2B and 2C) (Düvel et al., 2010; Choo et al., 2010; Csibi et al., 2013). Notably, the metabolite that changed the most between Ctrl and mutant kidneys at both P50 and P80 was fumarate (Figures 2D and 2E; Table S2), which we found accumulating up to the concentration of ~1 mM per kidney (Figure 2E). Fumarate is a metabolite with an average accumulation of ~4 mM in human *FH*-deficient renal cancers (Ternette et al., 2013; Tomlinson et al., 2002) and ~2 mM in animal models of *Fh1* renal inactivation (Ternette et al., 2013; Tomlinson et al., 2002). Targeted analysis of individual metabolites by liquid chromatography-mass spectrometry (LC-MS)

Figure 1. *T1$^{f/f}$:Cre* as a PRCC Mouse Model

(A) Kaplan-Meier survival curve of *T1$^{f/f}$:Cre* (n = 22) mice compared with *T1$^{f/+}$:Cre* and *Cre* controls (n = 22).

(B) Kidney over body (K/B) weight of *T1$^{f/f}$:Cre* mice and relative controls. We selected three different time points of analysis (P20, P50, and P80), where the K/B weight ratio increases dramatically. P20: n = 34 controls, n = 27 mutants; P50: n = 44 controls, n = 42 mutants; P80: n = 37 controls, n = 38 mutants. ANOVA followed by Tukey's multiple comparison test was performed. Data are shown as mean ± SD. ****$p < 0.0001$.

(C) Immunoblot for mTORC1 activation on *T1$^{f/f}$:Cre* kidney lysates compared with relative controls at P20, P50, and P80. pP70S6K^{T389} and pS6Rp$^{S240/244}$ and relative total protein were used to determine increased mTORC1 signaling, and vinculin was used as an internal loading control.

(D) H&E histological analysis of *T1$^{f/f}$:Cre* kidneys at three different time points. Cystogenesis arises at the first point of analysis (P20), whereas the disease progresses in cyst wall modification called papillae, cystadenomas (P50), and carcinomas (P80) (arrowhead). Scale bar, 100 μm.

(E) Number of cysts, cystadenomas and carcinomas counted in central longitudinal sections of n = 5 *T1$^{f/f}$:Cre* P80 kidneys. Data are shown as mean ± SD.

(F) Quantification of lesions inside *T1$^{f/f}$:Cre* kidney sections, dividing cortical from medullary region. Manifestations are expressed as cysts with papillae, cystadenomas, or carcinomas on total cysts. Data are shown as mean + SEM on n = 5 different samples for each time point, three sections each.

(G) Immunofluorescence (IF) analysis of *T1$^{f/f}$:Cre* and relative controls kidney slices against DBA (red) and Aquaporin1 (green) at P20 and P65. Scale bar, 100 μm.

(H) IHC for Ki67 on *T1$^{f/f}$:Cre* kidneys slices at P50 and P80. Scale bar, 100 μm.

(I) Quantification of Ki67 staining in (H). N = 9 sections (n = 3 fields for n = 3 sections of the same kidney) were counted for n = 3 *T1$^{f/f}$:Cre* kidneys at P50 and P80. ANOVA followed by Tukey's multiple comparison test was performed. Data are shown as mean +SD. **$p < 0.01$.

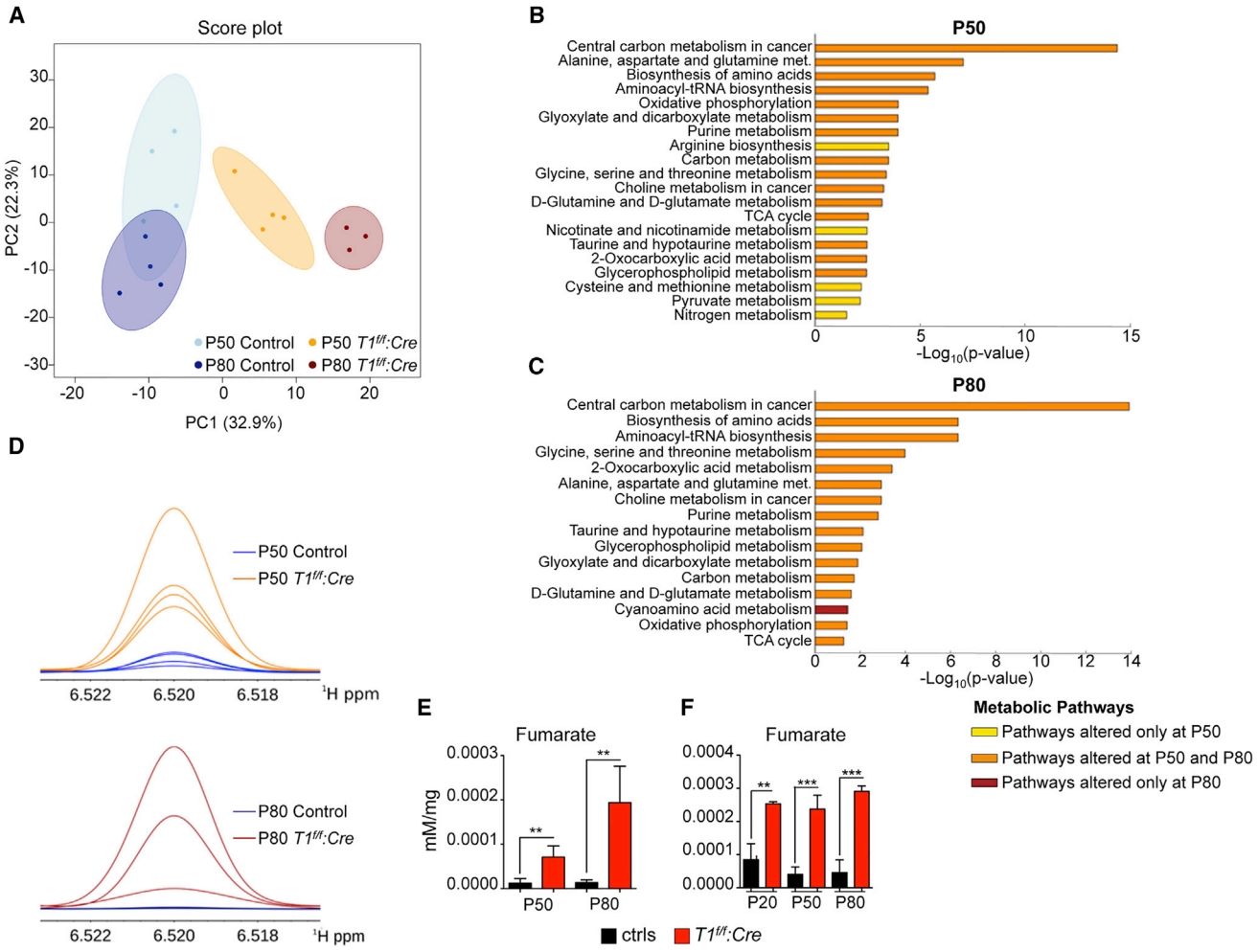

Figure 2. Metabolomic Analysis of *T1$^{f/f}$:Cre* Mice Revealed Fumarate Accumulation in Cortical Kidney Extracts

(A) Principal-component analysis (PCA) score plot of NMR metabolomics analysis of P50 and P80 mutant mice compared with relative controls. PCA shows good separation between cystic versus control groups in the kidney experiments. N = 4 P50 controls, n = 4 P50 mutants; n = 4 P80 controls, n = 3 P80 mutants.

(B and C) Results from over-representation analysis (ORA) at P50 (B) and P80 (C) show a cascade of metabolic impairments. Only KEGG pathways for which the adjusted p value is <0.05 are reported. Pathways are ordered according to p values. Yellow represents pathways that are enriched only at P50, orange pathways that are enriched both at P50 and P80, and red those enriched only at P80.

(D) Overlay of ^{1}H one-dimensional (1D) NMR spectra of P50 *T1$^{f/f}$:Cre* (orange) and P50 relative control (bright blue) renal cortices extracts (polar fraction) and of P80 *T1$^{f/f}$:Cre* (bordeaux) and P80 relative control (dark blue) renal cortices extracts, respectively. A zoom into the typical ^{1}H fumarate singlet at 6.52 ppm is shown.

(E) NMR quantification of fumarate on P50 and P80 *T1$^{f/f}$:Cre* kidney tissue analyzed in (A) compared with relative controls. Data are shown as mean + SD. Statistical analysis was performed using Student's unpaired two-tailed t test. **p < 0.01.

(F) LC-MS determination of fumarate analyzed in *T1$^{f/f}$:Cre* kidney tissue compared with relative controls at three different time points (P20, P50, and P80). N = 3 P20 controls, n = 3 P20 mutants, n = 6 P50 controls, n = 6 P50 mutants; n = 5 P80 controls, n = 5 P80 mutants. Data are shown as mean + SD. Statistical analysis was performed using Student's unpaired two-tailed t test between mutants and relative control quantifications. **p < 0.01 and ***p < 0.001.

confirmed the accumulation of fumarate at P20, P50, and P80 (Figure 2F). These data indicate that the oncometabolite fumarate specifically accumulates during tumor formation in *Tsc1*-mutant kidneys.

Fumarate Accumulation Correlates with Transformation in the *T1$^{f/f}$:Cre* Kidneys

We next investigated the contribution of fumarate accumulation to renal oncogenesis in *T1$^{f/f}$:Cre* animals. The oncogenic function of fumarate has been ascribed to multiple biological processes, including the succination of protein cysteine residues (Blatnik et al., 2008), inhibition of Ten-Eleven translocation (TET) DNA demethylases (Sciacovelli et al., 2016) (Figure 3A), and activation of the transcription factor HIF1α (Adam et al., 2011) (Figure S3A). In line with a significant accumulation of fumarate, 2-succinocysteine was found to be significantly accumulated in the *T1$^{f/f}$:Cre* kidneys at all three stages analyzed (P20, P50, and P80; Figure 3B). Increased levels of adenylosuccinate and argininosuccinate, two other metabolites accumulated in *Fh1*-deficient cells (Zheng et al., 2015), could be detected, further confirming

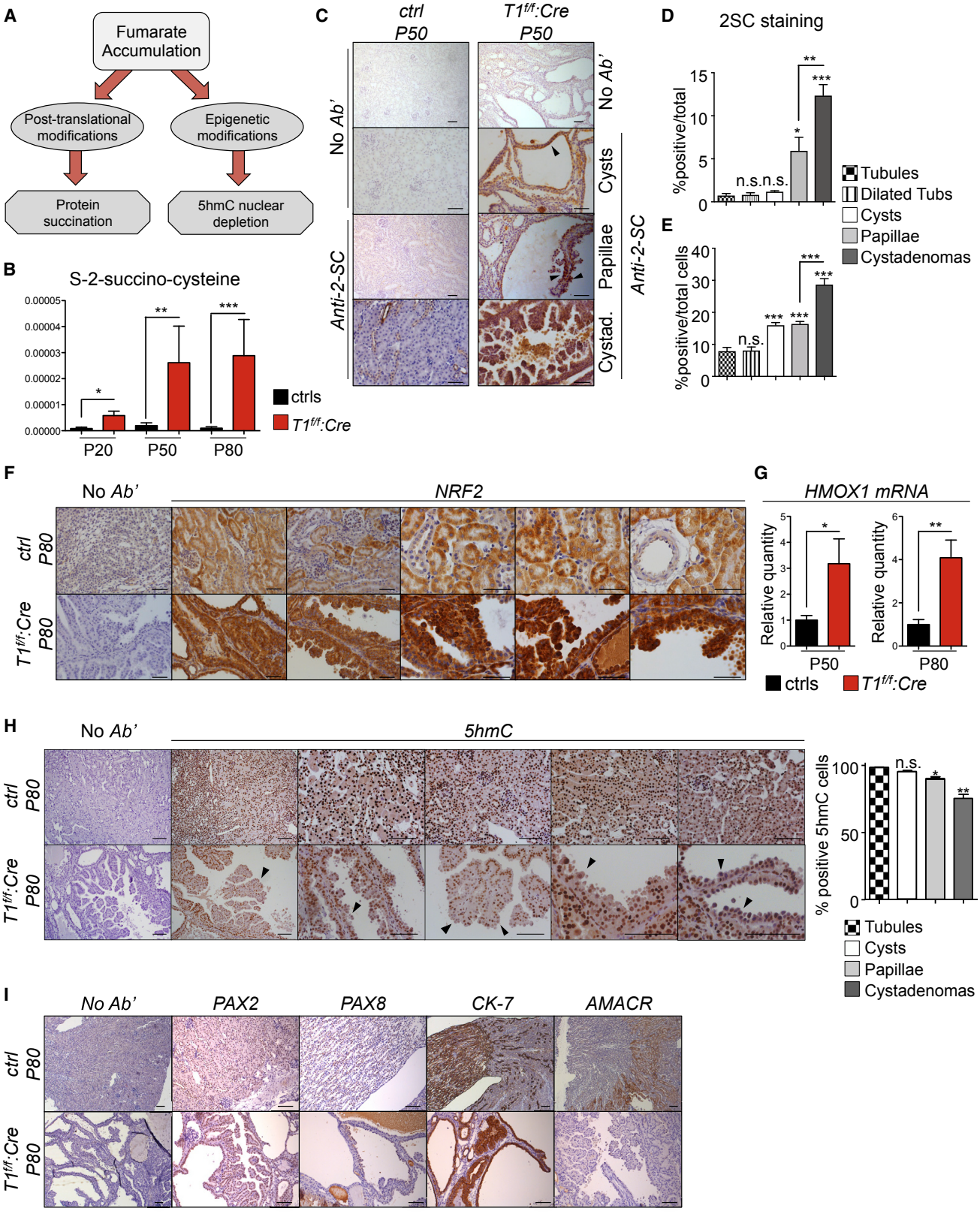

(legend on next page)

fumarate accumulation (Figure S3B). A previous study showed the accumulation of urea cycle intermediates in *Fh1*-mutant kidney tissues because of a shunt between the urea and TCA cycles (Adam et al., 2013). Indeed, analysis of the LC-MS spectra revealed a number of metabolic changes that also support this alteration in *T1$^{f/f}$:Cre* kidneys (Figures S3C and S3D). Furthermore, the levels of protein succination, a hallmark of FH loss (Bardella et al., 2011), were indeed confirmed by immunohistochemistry in *T1$^{f/f}$:Cre* kidneys (Figure 3C). Notably, whereas the cystic epithelium was only weakly stained, the epithelium lining the papillae and cystadenomas in *T1$^{f/f}$:Cre* kidneys was strongly positive for 2SC (Figure 3C). Quantification confirmed a small number of dilated tubules and cysts in which all cells were positive, comparable with controls (<1%; Figure 3D), and a significantly larger number of papillae and cystadenomas in which every cell of the structure was positive for staining (7% and 12%, respectively; Figure 3D), although a few, scattered positive cells could be detected in some cysts as well (Figure 3E). Among the established targets of protein succination is KEAP1, the negative regulator of the antioxidant master gene *NRF2* (Itoh et al., 1999; Ooi et al., 2011; Adam et al., 2011). Nrf2 was strongly expressed in the nucleus of cystadenomas and carcinoma cells (Figure 3F) and consistently increased expression of its direct target heme-oxygenase 1 (*Hmox1*) could be detected (Itoh et al., 1997) (Figure 3G). Next, we measured the levels of 5-hydroxy-methyl-cytosine (5hmC), as a readout of TET activity, using immunohistochemistry. This assay revealed a decreased signal in the nuclei of papillae and cystadenomas at P80 (Figure 3H). Finally, analysis of HIF1α levels revealed an upregulation of this transcription factor, which were reduced upon treatment with rapamycin (Figure S3E).

Overall, we showed that fumarate, progressively accumulated in *T1$^{f/f}$:Cre* kidneys, causes protein succination and the inhibition of DNA demethylation, two hallmarks of the oncogenic function of fumarate. Fumarate accumulation is a typical feature observed in the human syndrome hereditary leiomyomatosis and renal cell carcinoma (HLRCC) syndrome, caused by mutations of the *FH* gene (Tomlinson et al., 2002). Both familial and sporadic cases carrying mutations in *FH* are reported in humans, resulting in papillary type II RCC. Interestingly, we observed that *T1$^{f/f}$:Cre* kidney tissues were PAX2 positive, PAX8 negative, and AMACR negative, which excluded ccRCC and chromophobe subtype (crRCC) but were positive for Ck-7. This analysis is indicative of a PRCC subtype (Figure 3I), suggesting that our animals represent a model for papillary type II RCC.

mTORC1 Regulates *Fh1* Expression and Fumarate Accumulation in Murine Cells and Tissues

We next investigated the expression levels of *Fh1*, whose loss induced fumarate accumulation (Tomlinson et al., 2002) and type II PRCC. The qPCR and western blot (WB) analyses revealed that there is a nonsignificant downregulation of *Fh1* in *T1$^{f/f}$:Cre* kidneys at P20; however, at P50 and P80 the downregulation is highly significant, providing an explanation for the accumulation of fumarate (Figures 4A and S4A). Importantly, citrate synthase (*CS*) expression levels were unchanged, indicating that this regulation is specific and not secondary to a generic effect on mitochondrial enzymes (Figure S4B).

We next administered rapamycin *in vivo* at P30, prior to the transformation of the epithelia, and found that indeed this treatment was able to restore the expression levels of FH in the *T1$^{f/f}$:Cre* kidneys, with only a minimal effect on the kidney/body weight (Figures 4B and S4C). Next, we used *Tsc1*- and *Tsc2*-deficient mouse embryonic fibroblasts (*Tsc1$^{-/-}$* and *Tsc2$^{-/-}$*) and murine inner medullary collecting duct cells silenced for *Tsc1* (mIMCD^{shTsc1}) (Pema et al., 2016) compared with controls (*Tsc1$^{+/+}$* and *Tsc2$^{+/+}$* mouse embryonic fibroblasts [MEFs] and mIMCD^{shCtrl}, respectively). Fumarate accumulated in these cellular models upon loss of *Tsc1* or *Tsc2* to a final concentration of ~0.4 mM in IMCD cells and ~0.6 mM in MEFs (Figure 4C). Importantly, rapamycin, an established mTOR inhibitor, restored normal levels of fumarate in all these models (Figures 4C and S4D), suggesting that fumarate accumulation depends on mTORC1 activation. Thus, fumarate accumulation is one of the downstream effects of mTORC1 upregulation. Next, we examined whether the mTORC1 pathway also

Figure 3. Accumulation of Fumarate in *T1$^{f/f}$:Cre* Correlates with Disease Progression

(A) Representation of the pro-tumorigenic signals triggered by fumarate accumulation.

(B) LC-MS determination of S-2-succino-cysteine on *T1$^{f/f}$:Cre* kidney tissues analyzed as in Figure 2F compared with relative controls. Data are shown as mean + SD. Statistical analysis was performed using Student's unpaired two-tailed t test between mutants and relative controls quantifications. *p < 0.05, **p < 0.01, and ***p < 0.001.

(C) Anti-2-SC IHC staining on *T1$^{f/f}$:Cre* P50 kidneys compared with *T1$^{f/+}$:Cre* controls. Scale bar, 50 μm.

(D) Percentage of lesions in which 100% of the cells are positive for 2-SC IHC staining in *T1$^{f/f}$:Cre* kidneys at P50. Lesions were analyzed from n = 3 different sections from n = 3 mutant mice. Data are shown as mean + SD. ANOVA followed by Dunnett's multiple-comparison test was performed. n.s., not significant. *p < 0.05, **p < 0.01, ***p < 0.001.

(E) Percentage of positive 2-SC IHC cells in different lesions of *T1$^{f/f}$:Cre* kidneys at P50. Lesions were analyzed from n = 3 different sections from n = 3 mutant mice (excluding fully positive structures counted in C). Data are shown as mean + SD. ANOVA statistical analysis followed by Dunnett's multiple-comparison test was performed. n.s., not significant. ***p < 0.001.

(F) Anti-NRF2 IHC staining on *T1$^{f/f}$:Cre* P80 kidneys compared with *T1$^{f/+}$:Cre* controls. Scale, 50 μm.

(G) qRT-PCR analysis for *Hmox1* mRNA normalized to β-actin on *T1$^{f/f}$:Cre* kidneys at P50 and P80 compared with relative controls. N = 3 kidneys were analyzed for each time point condition. Data are shown as mean + SD. Statistical analysis was performed using Student's unpaired two-tailed t test. *p < 0.05 and **p < 0.01.

(H) Anti-5hmC IHC staining on *T1$^{f/f}$:Cre* P80 kidneys compared with *T1$^{f/+}$:Cre* controls. Arrowheads indicate nuclei with low positive staining in *T1$^{f/f}$:Cre* lesions. Scale bar, 100 μm. Data represent the percentage of positive nuclear stained cells on total cell number counted on the section per lesion. N = 3 controls (10 fields for each sample) and n = 3 P80 kidneys (10 complete structures for each sample). Data are shown as mean + SEM. Two-way ANOVA followed by Dunnett's post-test was performed (tubules group was used as control group). n.s., not significant. *p < 0.05 and **p < 0.01.

(I) IHC staining on *T1$^{f/f}$:Cre* and relative controls kidney for PAX2 and PAX8, CK-7, and AMACR (markers for ccRCC, PRCC, and crRCC, respectively). Scale bar, 50 μm.

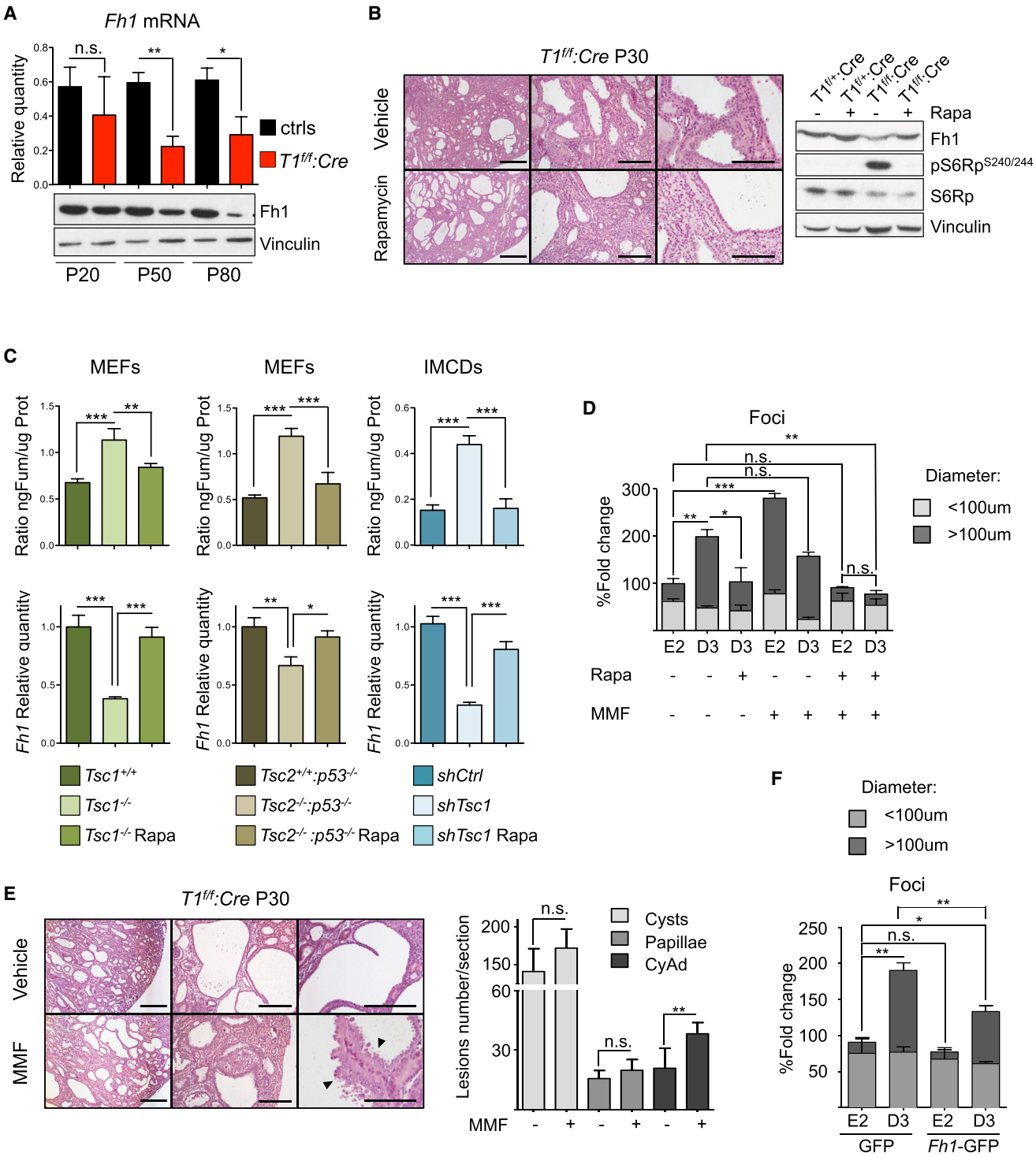

Figure 4. mTORC1 Regulates *Fh1* Expression and Fumarate Levels in Mice and Cells

(A) qRT-PCR and immunoblot analysis for Fh1 on *T1f/f:Cre* kidneys at P20, P50, and P80 compared with relative controls. mRNA was normalized to β-actin, extracted from n = 3 kidneys for each condition. Data are shown as mean + SD. ANOVA followed by Tukey's multiple comparison test was performed. n.s., not significant. *$p < 0.05$ and **$p < 0.01$. In WB, vinculin was used as loading control.

(B) Left: H&E staining of P30 *T1f/f:Cre* cortical kidney treated with rapamycin or vehicle. Scale bar, 100 μm. Right: immunoblot analysis for Fh1 expression levels and pS6Rp protein on *T1f/f:Cre* kidneys at P30 treated in the presence of rapamycin (+) or vehicle (-) compared with relative controls shows downregulation of Fh1 rescued by rapamycin treatment.

(legend continued on next page)

controls the expression of the tumor suppressor *Fh1* in cellular systems. Indeed, qPCR analysis revealed a significant downregulation of the *Fh1* transcript (but not the *CS* transcript) in all three cell lines described above, which was reversed upon treatment with rapamycin (Figures 4C and S4F). Similarly, FH protein levels are reduced in *Tsc1* cells and restored by rapamycin (Figure S4E). Of interest, chronic (72 hr) but not acute (24 hr) treatment with rapamycin achieved this effect (Figure S4G). These data indicate that fumarate accumulation in *Tsc1*-deficient animals and cells depends on the mTORC1-dependent suppression of *Fh1* expression.

Chronic mTORC1 Upregulation Leads to *Fh1* Downregulation and Fumarate Accumulation, which Contributes to Transformation in Renal Epithelia

We next investigated whether the downregulation of *Fh1* and subsequent accumulation of fumarate contribute to transformation in renal epithelia downstream of the mTORC1 pathway. To this end, we generated a renal epithelial cell line (mIMCD), where the *Tsc1* gene was ablated using the CRISPR/Cas9 system. Clones knocked out for the *Tsc1* gene were generated using three different single-guide RNAs. Clones transfected with each guide ($Tsc1^{-/-}$ mIMCD) or empty-vector controls (Ctrl mIMCD) were sorted, cultured, expanded, and analyzed using WB for the complete absence of hamartin expression and consequent mTORC1 upregulation, sensitive to rapamycin treatment (Figures S5A and S5B). Because renal epithelial cells are prone to anoikis when they detach from the substrate, we assessed their suitability to form foci in agar. When plated in agar, mIMCD cells die and form few colonies. In contrast, $Tsc1^{-/-}$ mIMCD cells were able to grow as large foci, and this effect was rescued by rapamycin or re-expression of *Tsc1* (Figures 4D, S5C, and S5D). Thus, we used this system to examine whether the exposure of cells to monomethyl fumarate (MMF; 100 μM, 4 times lower than the fumarate concentration in $Tsc1^{-/-}$ mIMCD), a cell-permeable analog of fumarate, is sufficient to drive foci formation. We subjected control (E2) and *Tsc1*-mutant (D3) clones to MMF for 24, 48, or 72 hr and tested whether this compound could induce the upregulation of *Hmox1* (Figure S5E). The exposure to MMF induced the significant upregulation of *Hmox1* transcript in both systems, indicating the activation of Nrf2 (Figure S5E). Next, we embedded controls (E2) and *Tsc1*-mutant cells (D3) in agar gels and treated the cells with MMF. The results showed that MMF treatment induced colony formation in control IMCD cells, whereas this treatment failed to enhance the effect in the *Tsc1*-mutant cells (Figures 4D and S5C). Exposure of IMCD cells to MMF in the presence of rapamycin, however, showed that colony formation is abrogated (Figure 4D). These data indicate that the exposure of normal epithelia to fumarate is sufficient to drive transformation, but that the role of mTORC1 in foci formation is broader than the effect of fumarate alone, as expected.

Next, we reasoned that treatment with MMF in pre-malignant lesions should accelerate the cancerous phenotype if this is indeed a mechanism contributing to transformation. Therefore, we treated $T1^{f/f}$*:Cre* mice (and relative controls) for 20 days with daily intra-peritoneal injections of 50 mg/kg MMF between P10 and P30, when cancerous lesions are low. Real-time PCR analysis of the collected kidneys revealed that control and mutant-treated kidneys displayed a higher level of *Hmox1* transcripts (Figure S5F), demonstrating that MMF reaches the kidney and achieves fumarate-associated antioxidant biological effects. Histological analysis revealed that MMF administration indeed increased the number of cystadenomas (Figures 4E and S5G). These data demonstrate that the increased fumarate accumulation drives a more malignant phenotype.

Finally, we reasoned that if the downregulation of *Fh1* downstream of mTORC1 is involved in driving transformation, it should be able to at least partially restore foci formation in the $Tsc1^{-/-}$ cells. Indeed, overexpression using a vector carrying *Fh1*-GFP, followed by fluorescence-activated cell sorting (FACS) and embedding in three-dimensional (3D) agar assays revealed that *Fh1*-GFP overexpression was able to reduce their foci formation potential, whereas the overexpression of *Fh1* had no effect on the control cell line (Figures 4F, S5H, and S5I). These data collectively show that fumarate can contribute to the transformation of normal renal epithelia, and *Fh1* repression downstream of mTORC1 plays an important role in the tumorigenic potential of *Tsc1* mutants. We conclude that this mechanism likely plays a role in the transformation of renal epithelia toward a cancerous phenotype in $T1^{f/f}$*:Cre* mice.

mTORC1 Upregulation Correlates with *FH* Downregulation and Fumarate Accumulation in Human RCC

Finally, we validated the link between mTORC1 upregulation and FH suppression in human samples. To test this hypothesis,

(C) Top: fumarate quantification on $Tsc1^{-/-}$ and $Tsc2^{-/-}$ MEFs and $mIMCD^{shTsc1}$ compared with relative control cells ± 72 hr rapamycin treatment (100 nM). Bottom: qRT-PCR analysis for *Fh1* mRNA normalized to *Arbp*, performed on mRNA extracted from $Tsc1^{-/-}$ and $Tsc2^{-/-}$ MEFs and $mIMCD^{shTsc1}$ compared with relative controls ± 72 hr rapamycin treatment (100 nM). Data are shown as mean + SD. ANOVA followed by Tukey's multiple comparison test was performed. Representative experiments of three different replicates. *$p < 0.05$, **$p < 0.01$, and ***$p < 0.001$.

(D) Foci count of soft agar assay performed on $Tsc1^{-/-}$ IMCDs (clone D3) compared with E2 control clone ± rapamycin treatment (100 nM) and ± MMF treatment (100 μm). Foci were divided according to diameter size, using 100 μm as a threshold. Data are represented as percentage of fold change compared with E2 clone foci count after 3 weeks of assay. Internal triplicates for each condition were used. Representative of n = 3 independent experiments. Data are shown as mean + SD. ANOVA followed by Tukey's multiple comparison test was performed. n.s., not significant. *$p < 0.05$, **$p < 0.01$, ***$p < 0.001$.

(E) Left: H&E staining of P30 $T1^{f/f}$*:Cre* MMF cortical kidney and untreated $T1^{f/f}$*:Cre*. Scale bar, 100 μm. Right: quantification of the lesions inside the samples are expressed as number of cysts, papillae, and cystadenomas counted per longitudinal section. Data are shown as mean + SD. $T1^{f/f}$*:Cre* untreated n = 5, $T1^{f/f}$*:Cre* MMF n = 6, three section each. ANOVA followed by Tukey's multiple-comparison test was performed. n.s., not significant. **$p < 0.01$.

(F) Foci count of soft agar assay performed on $Tsc1^{-/-}$*IMCDs* (clone D3) compared with E2 control clone transfected with *GFP* or *Fh1-GFP* plasmid and sorted after 1 week for positive expression levels. Foci were divided according to diameter size, using 100 μm as a threshold. Data are represented as percentage of fold change compared with E2-GFP clone foci count after 3 weeks of assay. Internal triplicates for each condition were used. Representative of n = 3 independent experiments. Data are shown as mean + SD. ANOVA followed by Tukey's multiple comparison test was performed. n.s., not significant.*$p < 0.05$ and **$p < 0.01$.

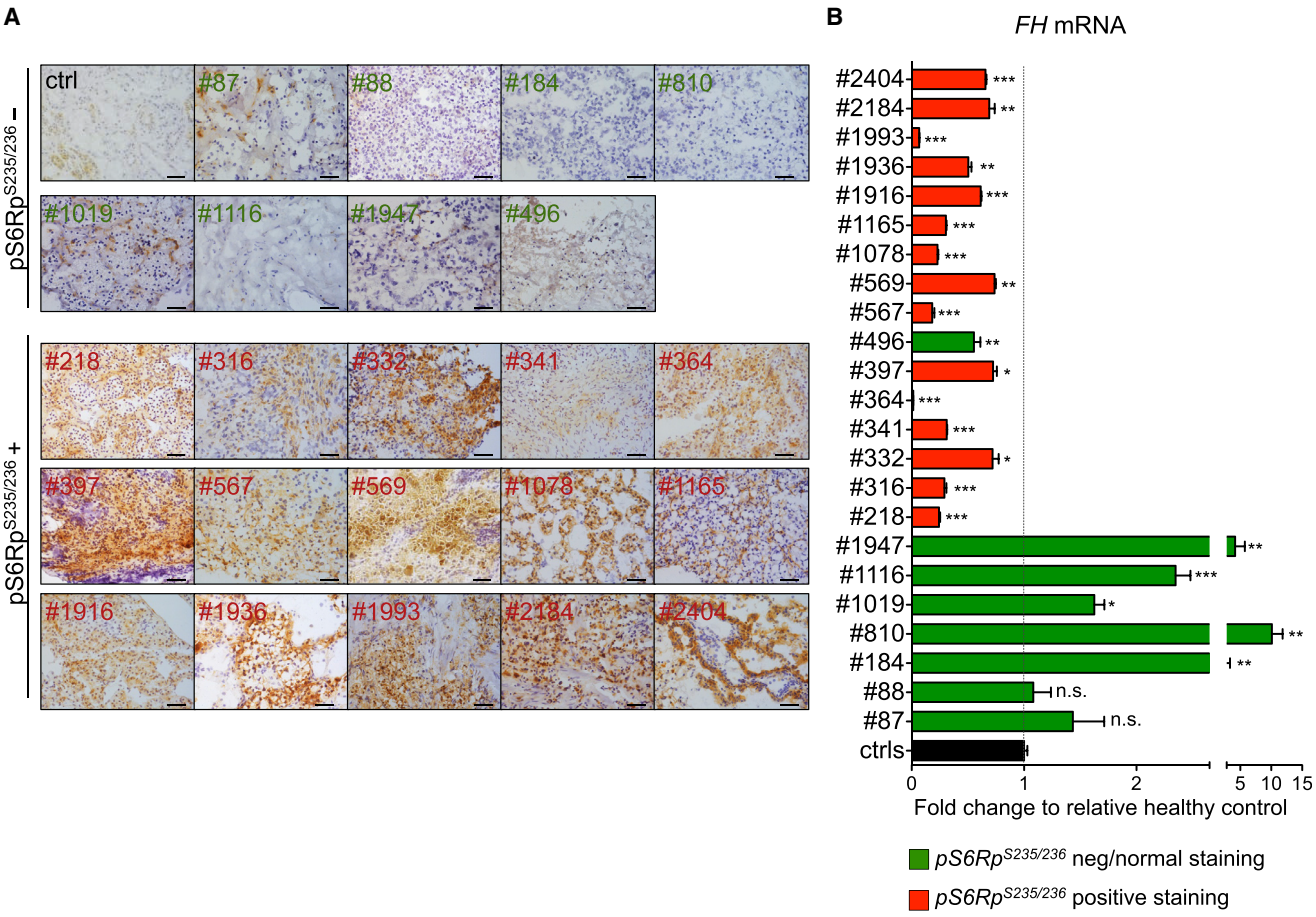

Figure 5. mTORC1 Activation Correlates with *FH* Downregulation in Human ccRCC

(A) Panel of pS6Rp$^{S235/236}$ IHC staining in n = 23 ccRCC patient nephrectomies compared with healthy kidney tissue derived from the same kidney. Samples with green number do not show increased staining compared with healthy control. Samples with red numbers have variable increased staining. Scale bar, 50 μm. A representative image from each sample is shown.

(B) qRT-PCR analysis for *FH* mRNA normalized to *H3* on tumoral tissue obtained from the 23 ccRCC samples analyzed in Figure S6A compared with relative internal control (healthy kidney tissue). Data are shown as mean + SEM of three different replicates. ANOVA followed by Dunnett's multiple-comparison test was performed. n.s., not significant. *p < 0.05, **p < 0.01, and ***p < 0.001.

we analyzed primary samples from renal ccRCC obtained from consenting patients submitted to nephrectomy (see STAR Methods). We restricted the study to samples for which both optimal cutting temperature (OCT)-embedded and frozen tissue pellets from nephrectomized cancerous lesion and control non-cancerous tissues were available. A total of 15 of 23 cancer samples displayed increased positive staining for pS6Rp (approximately 65%), confirming mTORC1 upregulation in a large proportion of ccRCC (Figure 5A). Among the 23 samples analyzed, 16 samples showed downregulation of *FH* mRNA levels compared with relative healthy tissue (Figure 5B), and these samples also exhibited high mTORC1 activation (with the one exception of sample 496) (Figures 5A and 5B). Moreover, to determine whether *FH* downregulation correlates with increased NRF2 levels, as in the mouse, we performed immunohistochemistry (IHC) on OCT-embedded samples (Figure S6A). Interestingly, 15 of 16 samples with lower *FH* mRNA showed higher NRF2 staining compared with controls (Figure S6B). These data suggest a direct link between the activation of the mTORC1 pathway and the reduced abundance of *FH* mRNA in patients, supporting the idea that mTORC1 directly regulates the expression levels of *FH*.

Concluding Remarks

In the present study, we describe a mouse model of renal carcinogenesis faithfully recapitulating type II PRCC. Previous studies reported that inactivation of individual oncosuppressors in the kidney typically mutated in human RCC results in aggressive and fulminant polycystic kidney disease, rather than progression to cancer (Frew et al., 2008; Baba et al., 2008; Pollard et al., 2007; Zhou et al., 2009; Traykova-Brauch et al., 2008). However, recent studies highlight the potential of modeling ccRCC in mice through combination of mutations in multiple tumor suppressors (Gu et al., 2017; Harlander et al., 2017). In the present study we find that inactivation of a single tumor suppressor gene (*Tsc1*) using a KspCre line developed a mild progression of renal

cystogenesis, likely providing sufficient time for transformation, even in the absence of inactivation of multiple genes. However, because our study shows that *Fh1* is downregulated in response to mTORC1 chronic upregulation, one possibility is that the cross-talk between *Tsc1* and *Fh1* genes might be relevant for tumor manifestation and that the regulation of *Fh1* levels by mTORC1 might result in a "functional haploinsufficiency" resulting in reduced activity of two distinct tumor suppressors, leading to tumor development.

In conclusion, in this study, we demonstrated that the chronic activation of mTORC1 in the distal tubules and collecting ducts of the kidney is sufficient to drive the progressive transformation of benign lesions into cancers in mice. Mechanistically, mTORC1 activation results in the downregulation of *Fh1* and the subsequent accumulation of the oncometabolite fumarate, likely involved in the transformation. These data provide a causal link between the metabolic derangement downstream of mTORC1 and carcinogenesis in the kidney.

STAR★METHODS

Detailed methods are provided in the online version of this paper and include the following:

- KEY RESOURCES TABLE
- CONTACT FOR REAGENT AND RESOURCES SHARING
- EXPERIMENTAL MODEL AND SUBJECT DETAILS
  - Cell lines
  - Mice
  - Human RCC tissues
- METHOD DETAILS
  - Antibodies and Inhibitors
  - *In vivo* treatment
  - Histological analysis, immunofluorescence and immunohistochemistry
  - Cyst structures quantification analysis
  - Metabolomic NMR analysis
  - LC-MS Metabolomic analysis
  - KEGG-Pathways Based Overrepresentation Analysis (ORA)
  - *In vitro* Fumarate quantification
  - Estimation of Fumarate concentration
  - Soft-agar foci assay
  - Real-Time PCR analysis
  - Western blot analysis
- QUANTIFICATION AND STATISTICAL ANALYSIS
- DATA AND SOFTWARE AVAILABILITY

SUPPLEMENTAL INFORMATION

Supplemental Information includes six figures and three tables and can be found with this article online at https://doi.org/10.1016/j.celrep.2018.06.106.

ACKNOWLEDGMENTS

We are grateful to other members of the Boletta lab for helpful discussions, to F. Sanvito and the Pathology Unit of San Raffaele for the evaluation of the cancerous lesions and for the design of markers of different RCC types, to the San Raffaele Mouse Histopathology Facility (A. Fiocchi) to the San Raffaele advanced microscopy laboratory (ALEMBIC) and to P.J. Pollard and N. Frizzell for the anti-2-SC antibody. This work was funded by the Italian Association for Research on Cancer (AIRC; grants IG14382 and IG18706 to A.B.) and by the Umberto Veronesi Foundation (post-doctoral fellowship to R.P.). C.F. and A.S.H.C. are supported by a Medical Research Council (MRC) Core Award to the MRC Cancer Unit.

AUTHOR CONTRIBUTIONS

L.D. and E.A.N. designed the studies, performed experiments, analyzed data, and wrote the manuscript. V.M. designed, performed, and interpreted the NMR metabolomics data. R.P. performed bioinformatics analysis of mass spectrometry data. M.P. performed the initial crossings of *Tsc1*-mutant mice and analyzed kidneys. A.S.H.C. and E.G. performed mass spectrometry metabolomics analysis, interpreted data, and suggested experiments. F.B., A.L., F.M., and U.C. collected clinical data and samples, selected the specimens to be analyzed, interpreted the results, and wrote the clinical part of the manuscript. M.C. performed animal crossings and analyzed some histological data. G.M. supervised the NMR metabolomics studies. C.F. supervised the mass spectrometry metabolomics analysis, discussed them and suggested new experiments, and provided reagents. A.B. designed the studies, supervised the work and collaborations, and wrote the manuscript.

DECLARATION OF INTERESTS

The authors declare no competing interests.

Received: January 22, 2018
Revised: June 4, 2018
Accepted: June 27, 2018
Published: July 31, 2018

REFERENCES

Adam, J., Hatipoglu, E., O'Flaherty, L., Ternette, N., Sahgal, N., Lockstone, H., Baban, D., Nye, E., Stamp, G.W., Wolhuter, K., et al. (2011). Renal cyst formation in Fh1-deficient mice is independent of the Hif/Phd pathway: roles for fumarate in KEAP1 succination and Nrf2 signaling. Cancer Cell *20*, 524–537.

Adam, J., Yang, M., Bauerschmidt, C., Kitagawa, M., O'Flaherty, L., Maheswaran, P., Özkan, G., Sahgal, N., Baban, D., Kato, K., et al. (2013). A role for cytosolic fumarate hydratase in urea cycle metabolism and renal neoplasia. Cell Rep. *3*, 1440–1448.

Baba, M., Furihata, M., Hong, S.B., Tessarollo, L., Haines, D.C., Southon, E., Patel, V., Igarashi, P., Alvord, W.G., Leighty, R., et al. (2008). Kidney-targeted Birt-Hogg-Dube gene inactivation in a mouse model: Erk1/2 and Akt-mTOR activation, cell hyperproliferation, and polycystic kidneys. J. Natl. Cancer Inst. *100*, 140–154.

Bardella, C., El-Bahrawy, M., Frizzell, N., Adam, J., Ternette, N., Hatipoglu, E., Howarth, K., O'Flaherty, L., Roberts, I., Turner, G., et al. (2011). Aberrant succination of proteins in fumarate hydratase-deficient mice and HLRCC patients is a robust biomarker of mutation status. J. Pathol. *225*, 4–11.

Ben-Sahra, I., Howell, J.J., Asara, J.M., and Manning, B.D. (2013). Stimulation of de novo pyrimidine synthesis by growth signaling through mTOR and S6K1. Science *339*, 1323–1328.

Bjornsson, J., Short, M.P., Kwiatkowski, D.J., and Henske, E.P. (1996). Tuberous sclerosis-associated renal cell carcinoma. Clinical, pathological, and genetic features. Am. J. Pathol. *149*, 1201–1208.

Blatnik, M., Frizzell, N., Thorpe, S.R., and Baynes, J.W. (2008). Inactivation of glyceraldehyde-3-phosphate dehydrogenase by fumarate in diabetes: formation of S-(2-succinyl)cysteine, a novel chemical modification of protein and possible biomarker of mitochondrial stress. Diabetes *57*, 41–49.

Brugarolas, J. (2014). Molecular genetics of clear-cell renal cell carcinoma. J. Clin. Oncol. *32*, 1968–1976.

Calcagnì, A., Kors, L., Verschuren, E., De Cegli, R., Zampelli, N., Nusco, E., Confalonieri, S., Bertalot, G., Pece, S., Settembre, C., et al. (2016). Modelling TFE renal cell carcinoma in mice reveals a critical role of WNT signaling. eLife *5*, 5.

Capitanio, U., and Montorsi, F. (2016). Renal cancer. Lancet *387*, 894–906.

Choo, A.Y., Kim, S.G., Vander Heiden, M.G., Mahoney, S.J., Vu, H., Yoon, S.O., Cantley, L.C., and Blenis, J. (2010). Glucose addiction of TSC null cells is caused by failed mTORC1-dependent balancing of metabolic demand with supply. Mol. Cell *38*, 487–499.

Chow, W.H., Dong, L.M., and Devesa, S.S. (2010). Epidemiology and risk factors for kidney cancer. Nat. Rev. Urol. *7*, 245–257.

Csibi, A., Fendt, S.M., Li, C., Poulogiannis, G., Choo, A.Y., Chapski, D.J., Jeong, S.M., Dempsey, J.M., Parkhitko, A., Morrison, T., et al. (2013). The mTORC1 pathway stimulates glutamine metabolism and cell proliferation by repressing SIRT4. Cell *153*, 840–854.

Dibble, C.C., Elis, W., Menon, S., Qin, W., Klekota, J., Asara, J.M., Finan, P.M., Kwiatkowski, D.J., Murphy, L.O., and Manning, B.D. (2012). TBC1D7 is a third subunit of the TSC1-TSC2 complex upstream of mTORC1. Mol. Cell *47*, 535–546.

Distefano, G., Boca, M., Rowe, I., Wodarczyk, C., Ma, L., Piontek, K.B., Germino, G.G., Pandolfi, P.P., and Boletta, A. (2009). Polycystin-1 regulates extracellular signal-regulated kinase-dependent phosphorylation of tuberin to control cell size through mTOR and its downstream effectors S6K and 4EBP1. Mol. Cell. Biol. *29*, 2359–2371.

Düvel, K., Yecies, J.L., Menon, S., Raman, P., Lipovsky, A.I., Souza, A.L., Triantafellow, E., Ma, Q., Gorski, R., Cleaver, S., et al. (2010). Activation of a metabolic gene regulatory network downstream of mTOR complex 1. Mol. Cell *39*, 171–183.

Frew, I.J., Thoma, C.R., Georgiev, S., Minola, A., Hitz, M., Montani, M., Moch, H., and Krek, W. (2008). pVHL and PTEN tumour suppressor proteins cooperatively suppress kidney cyst formation. EMBO J. *27*, 1747–1757.

Gaude, E., Chignola, F., Spiliotopoulos, D., Spitaleri, A., Ghitti, M., Garcia-Manteiga, J.M., Mari, S., and Musco, G. (2013). muma, an R package for metabolomics univariate and multivariate statistical analysis. Curr. Metabolom. *1*, 180–189.

Goodpaster, A.M., Romick-Rosendale, L.E., and Kennedy, M.A. (2010). Statistical significance analysis of nuclear magnetic resonance-based metabonomics data. Anal. Biochem. *401*, 134–143.

Gu, Y.F., Cohn, S., Christie, A., McKenzie, T., Wolff, N.C., Do, Q.N., Madhuranthakam, A., Pedrosa, I., Wang, T., Dey, A., et al. (2017). Modeling renal cell carcinoma in mice: Bap1 and Pbrm1 inactivation drive tumor grade. Cancer Discov. *7*, 900–917.

Guertin, D.A., and Sabatini, D.M. (2007). Defining the role of mTOR in cancer. Cancer Cell *12*, 9–22.

Harlander, S., Schönenberger, D., Toussaint, N.C., Prummer, M., Catalano, A., Brandt, L., Moch, H., Wild, P.J., and Frew, I.J. (2017). Combined mutation in Vhl, Trp53 and Rb1 causes clear cell renal cell carcinoma in mice. Nat. Med. *23*, 869–877.

Itoh, K., Chiba, T., Takahashi, S., Ishii, T., Igarashi, K., Katoh, Y., Oyake, T., Hayashi, N., Satoh, K., Hatayama, I., et al. (1997). An Nrf2/small Maf heterodimer mediates the induction of phase II detoxifying enzyme genes through antioxidant response elements. Biochem. Biophys. Res. Commun. *236*, 313–322.

Itoh, K., Wakabayashi, N., Katoh, Y., Ishii, T., Igarashi, K., Engel, J.D., and Yamamoto, M. (1999). Keap1 represses nuclear activation of antioxidant responsive elements by Nrf2 through binding to the amino-terminal Neh2 domain. Genes Dev. *13*, 76–86.

Kwiatkowski, D.J., Zhang, H., Bandura, J.L., Heiberger, K.M., Glogauer, M., el-Hashemite, N., and Onda, H. (2002). A mouse model of TSC1 reveals sex-dependent lethality from liver hemangiomas, and up-regulation of p70S6 kinase activity in Tsc1 null cells. Hum. Mol. Genet. *11*, 525–534.

Lin, C.Y., Wu, H.F., Tjeerdema, R.S., and Viant, M.R. (2007). Evaluation of metabolite extraction strategies from tissue samples using NMR metabolomics. Metabolomics *3*, 55–67.

Menon, S., Yecies, J.L., Zhang, H.H., Howell, J.J., Nicholatos, J., Harputlugil, E., Bronson, R.T., Kwiatkowski, D.J., and Manning, B.D. (2012). Chronic activation of mTOR complex 1 is sufficient to cause hepatocellular carcinoma in mice. Sci. Signal. *5*, ra24.

Nagai, R., Brock, J.W., Blatnik, M., Baatz, J.E., Bethard, J., Walla, M.D., Thorpe, S.R., Baynes, J.W., and Frizzell, N. (2007). Succination of protein thiols during adipocyte maturation: a biomarker of mitochondrial stress. J. Biol. Chem. *282*, 34219–34228.

Onda, H., Lueck, A., Marks, P.W., Warren, H.B., and Kwiatkowski, D.J. (1999). Tsc2(+/-) mice develop tumors in multiple sites that express gelsolin and are influenced by genetic background. J. Clin. Invest. *104*, 687–695.

Ooi, A., Wong, J.C., Petillo, D., Roossien, D., Perrier-Trudova, V., Whitten, D., Min, B.W., Tan, M.H., Zhang, Z., Yang, X.J., et al. (2011). An antioxidant response phenotype shared between hereditary and sporadic type 2 papillary renal cell carcinoma. Cancer Cell *20*, 511–523.

Pema, M., Drusian, L., Chiaravalli, M., Castelli, M., Yao, Q., Ricciardi, S., Somlo, S., Qian, F., Biffo, S., and Boletta, A. (2016). mTORC1-mediated inhibition of polycystin-1 expression drives renal cyst formation in tuberous sclerosis complex. Nat. Commun. *7*, 10786.

Pollard, P.J., Spencer-Dene, B., Shukla, D., Howarth, K., Nye, E., El-Bahrawy, M., Deheragoda, M., Joannou, M., McDonald, S., Martin, A., et al. (2007). Targeted inactivation of fh1 causes proliferative renal cyst development and activation of the hypoxia pathway. Cancer Cell *11*, 311–319.

Pugh, C.W., and Ratcliffe, P.J. (2003). Regulation of angiogenesis by hypoxia: role of the HIF system. Nat. Med. *9*, 677–684.

Sciacovelli, M., Gonçalves, E., Johnson, T.I., Zecchini, V.R., da Costa, A.S., Gaude, E., Drubbel, A.V., Theobald, S.J., Abbo, S.R., Tran, M.G., et al. (2016). Fumarate is an epigenetic modifier that elicits epithelial-to-mesenchymal transition. Nature *537*, 544–547.

Shao, X., Somlo, S., and Igarashi, P. (2002). Epithelial-specific Cre/lox recombination in the developing kidney and genitourinary tract. J. Am. Soc. Nephrol. *13*, 1837–1846.

Shroff, E.H., Eberlin, L.S., Dang, V.M., Gouw, A.M., Gabay, M., Adam, S.J., Bellovin, D.I., Tran, P.T., Philbrick, W.M., Garcia-Ocana, A., et al. (2015). MYC oncogene overexpression drives renal cell carcinoma in a mouse model through glutamine metabolism. Proc. Natl. Acad. Sci. U S A *112*, 6539–6544.

Tee, A.R., Fingar, D.C., Manning, B.D., Kwiatkowski, D.J., Cantley, L.C., and Blenis, J. (2002). Tuberous sclerosis complex-1 and -2 gene products function together to inhibit mammalian target of rapamycin (mTOR)-mediated downstream signaling. Proc. Natl. Acad. Sci. U S A *99*, 13571–13576.

Ternette, N., Yang, M., Laroyia, M., Kitagawa, M., O'Flaherty, L., Wolhulter, K., Igarashi, K., Saito, K., Kato, K., Fischer, R., et al. (2013). Inhibition of mitochondrial aconitase by succination in fumarate hydratase deficiency. Cell Rep. *3*, 689–700.

Tomlinson, I.P., Alam, N.A., Rowan, A.J., Barclay, E., Jaeger, E.E., Kelsell, D., Leigh, I., Gorman, P., Lamlum, H., Rahman, S., et al.; Multiple Leiomyoma Consortium (2002). Germline mutations in FH predispose to dominantly inherited uterine fibroids, skin leiomyomata and papillary renal cell cancer. Nat. Genet. *30*, 406–410.

Toro, J.R., Nickerson, M.L., Wei, M.H., Warren, M.B., Glenn, G.M., Turner, M.L., Stewart, L., Duray, P., Tourre, O., Sharma, N., et al. (2003). Mutations in the fumarate hydratase gene cause hereditary leiomyomatosis and renal cell cancer in families in North America. Am. J. Hum. Genet. *73*, 95–106.

Traykova-Brauch, M., Schönig, K., Greiner, O., Miloud, T., Jauch, A., Bode, M., Felsher, D.W., Glick, A.B., Kwiatkowski, D.J., Bujard, H., et al. (2008). An efficient and versatile system for acute and chronic modulation of renal tubular function in transgenic mice. Nat. Med. *14*, 979–984.

Wilson, C., Idziaszczyk, S., Parry, L., Guy, C., Griffiths, D.F., Lazda, E., Bayne, R.A., Smith, A.J., Sampson, J.R., and Cheadle, J.P. (2005). A mouse model of tuberous sclerosis 1 showing background specific early post-natal mortality and metastatic renal cell carcinoma. Hum. Mol. Genet. *14*, 1839–1850.

Xia, J., Bjorndahl, T.C., Tang, P., and Wishart, D.S. (2008). MetaboMiner–semi-automated identification of metabolites from 2D NMR spectra of complex biofluids. BMC Bioinformatics *9*, 507.

Zheng, L., Cardaci, S., Jerby, L., MacKenzie, E.D., Sciacovelli, M., Johnson, T.I., Gaude, E., King, A., Leach, J.D., Edrada-Ebel, R., et al. (2015). Fumarate induces redox-dependent senescence by modifying glutathione metabolism. Nat. Commun. *6*, 6001.

Zhou, J., Brugarolas, J., and Parada, L.F. (2009). Loss of Tsc1, but not Pten, in renal tubular cells causes polycystic kidney disease by activating mTORC1. Hum. Mol. Genet. *18*, 4428–4441.

STAR★METHODS

KEY RESOURCES TABLE

REAGENT or RESOURCE	SOURCE	IDENTIFIER
Antibodies		
Rabbit polyclonal anti-pP70S6K Thr389	Cell Signaling Technology	Cat#9205
Rabbit polyclonal anti-pS6Rp Ser240/244	Cell Signaling Technology	Cat#2215
Rabbit polyclonal anti-pS6Rp Ser235/236	Cell Signaling Technology	Cat#2211
Rabbit polyclonal anti-S6RP	Cell Signaling Technology	Cat#2217
Rabbit polyclonal anti-TSC1	Cell Signaling Technology	Cat#4906; RIDD: AB_2209790
Rabbit polyclonal anti-pAKT Thr308	Cell Signaling Technology	Cat#9275
Rabbit polyclonal anti-pAKT Ser243	Cell Signaling Technology	Cat#9271
Rabbit polyclonal anti-pERK Thr202/Tyr204	Cell Signaling Technology	Cat#9101
Rabbit polyclonal anti-AKT	Cell Signaling Technology	Cat#9272; RIDD: AB_329827
Rabbit polyclonal anti-ERK	Cell Signaling Technology	Cat#9102
Rabbit polyclonal anti-P70S6K C-18	Santa Cruz Biotechnology	Cat#sc-230
Mouse monoclonal anti-Fh1 H-6	Santa Cruz Biotechnology	Cat#sc-393992
Mouse monoclonal anti-Vinculin V284	Millipore	Cat#05-386; RIDD:AB_11212640
Rabbit polyclonal anti-HIF1α	Cayman Chemical Company	Cat#10006421
Rabbit monoclonal anti-PAX2 [EP3251]	Abcam	Cat#ab79389; RIDD:AB_1603338
Mouse monoclonal anti-PAX8 [PAX8R1]	Abcam	Cat#ab53490; RIDD:AB_2267905
Rabbit monoclonal anti-Cytokeratin7 [EPR17078]	Abcam	Cat#ab181598
Rabbit monoclonal anti-Nrf2 [EP1808Y]	Abcam	Cat#ab62352
Rabbit monoclonal anti-Ki67	Thermo Fisher Scientific	Cat#RM-9106
Mouse monoclonal anti-AMACR	Novus Biologicals	Cat#NBP2-45491
Rabbit polyclonal anti-5hmC	Active Motif	Cat#V1339769
Rabbit polyclonal anti-2SC	Nagai et al., 2007	N.A.
Donkey polyclonal anti-rabbit HRP linked	GE Amersham	Cat#NXA934
Sheep polyclonal anti-mouse HRP linked	GE Amersham	Cat#NXA931
Biological Samples		
Human RCC tissues	San Raffaele URI Biobank	(protocol URBBAN, IRB approval Sept. 2010)
Chemicals, Peptides, and Recombinant Proteins		
Rapamycin	LC Laboratories	Cat#R-5000
MMF	Sigma-Aldrich	Cat#651419
Cobalt chloride	Sigma-Aldrich	Cat#232696
LTL	Vector Laboratories	Cat#FL-1321
DBA	Vector Laboratories	Cat#RL-1032
DAPI	Santa Cruz Biotechnology	Cat# sc-3598
NucleoZOL reagent	Macherey-Nagel	Cat#740404.200
Oligo(dt)15 primers	Promega	Cat#C1101
ImProm-II Reverse Transcriptase	Promega	Cat#A3802
SYBR Green I master mix	Roche	Cat#04707516001
Biorad Protein Assay	Biorad	Cat#500-0006
Lipofectamine 2000	Invitrogen	Cat#12566014
Critical Commercial Assays		
Fumarate Colorimetric Assay	BioVision	Cat#K633-100
RNAspin Mini kit	GE Healthcare	Cat#25-0500-72

(*Continued on next page*)

Continued		
REAGENT or RESOURCE	SOURCE	IDENTIFIER
Experimental Models: Cell Lines		
Tsc1$^{-/-}$ MEFs	Kwiatkowski et al., 2002	N/A
Tsc2$^{-/-}$:*p53*$^{-/-}$ MEFs	Kwiatkowski et al., 2002	N/A
mIMCD^{shTsc1}	Pema et al., 2016	N/A
mIMCD*Tsc1*$^{-/-}$	This paper	N/A
Experimental Models: Organisms/Strains		
Mouse: *Tsc1*$^{f/f}$:*KspCre* (C57BL6 background)	Pema et al., 2016	N/A
Mouse: *Tsc1*$^{f/+}$:*KspCre* (C57BL6 background)	Pema et al., 2016	N/A
Mouse: *Tsc1*$^{+/+}$:*KspCre* (C57BL6 background)	Pema et al., 2016	N/A
Oligonucleotides		
See Table S1 for qRT-PCR primer sequences	Eurofin	N/A
Recombinant DNA		
Fh1-GFP plasmid	Sciacovelli et al., 2016	N/A
Tsc1-Flag plasmid	Distefano et al., 2009	Addgene
pEGFP-NI plasmid	Clontech	Cat#6085-1
Cas9-RFP plasmid	Sigma-Aldrich	Cat#Cas9RFPP-1EA
Tsc1 guide sgRNA1: CCTATGCTTGTCAACACGTTGG	Sigma-Aldrich	#MM0000384339
Tsc1 guide sgRNA2: CCAATTCTCAGCCGGTATTGCA	Sigma-Aldrich	#MM0000384341
Software and Algorithms		
XCalibur Qual Browser	Thermo Fisher Scientific	N/A
XCalibur Quan Browser	Thermo Fisher Scientific	N/A
ImageJ	NIH	http://rsb.info.nih.gov/ij/
Prism 5 Software	GraphPad	https://www.graphpad.com/
Chenomx 7.7	Chenomx Inc.	N/A
Metabominer	Xia et al., 2008	N/A
MATLAB®	MathWorks	https://www.mathworks.com
R	R Development Core Team	N/A
KEGG-Pathways Based Overrepresentation Analysis	This paper	https://www.r-project.org
Other		
Mouse Diet	Chow diet	Cat#C25/18CR

CONTACT FOR REAGENT AND RESOURCES SHARING

Further information and requests for resources and reagents should be directed to and will be fulfilled by the Lead Contact, Alessandra Boletta (boletta.alessandra@hsr.it).

EXPERIMENTAL MODEL AND SUBJECT DETAILS

Cell lines

Mouse embryonic fibroblasts (MEFs) derived from *Tsc1*$^{-/-}$ embryos or *Tsc2*$^{-/-}$:*p53*$^{-/-}$ embryos were kindly provided by Dr. Kwiatkowski (Kwiatkowski et al., 2002) and previously used in Pema et al. (Pema et al., 2016). The mIMCD cells carrying shRNA against the *Tsc1* gene were previously described (Pema et al., 2016). To generate the *Tsc1* KO (*T1*$^{-/-}$) mIMCD cells we used the CRISPR-Cas9 technology and transfected cells with plasmid carrying Cas9 endonuclease cDNA and one of two independent sgRNA guides specific for exons of the *Tsc1* gene (or empty sequence #CAS9RFP-1EA for control clones) provided by Sigma-Aldrich (see the sequences below). 4*10^5 mIMCD cells were seeded and 24 h later transfected with the respective plasmid using Lipofectamine 2000 (Invitrogen, #12566014) as manufactured instructions (Ratio DNA/Lipofectamine 1:3). Three days after cells were sorted for GFP (RFP for controls) positive fluorescence, collected as single cell in a 96 multiwell and expanded. Clones were analyzed for *Tsc1* expression. Three clones knock-out for *Tsc1* gene (A9, D3 and F12) and control clones were selected for further use. sgRNA1: CCTATGCTTGT CAACACGTTGG (Product #MM0000384339); sgRNA2: CCAATTCTCAGCCGGTATTGCA (Product #MM0000384341).

Mice

To generate *Tsc1*$^{f/f}$*:KspCre* mice we intercrossed *Tsc1*$^{f/+}$*:KspCre* mice (Pema et al., 2016). All the mice used in these experiments were in pure C57BL6 genetic background (backcrossed over ten times). All animal care and experimental protocols were conducted after approval of a specific protocol (IACUC-736) by the institutional care and use ethical committee at the San Raffaele Scientific Institute, further approved by the Italian Ministry of Health. The age of analysis is indicated in the text and legends. The gender was distributed as half and half.

Human RCC tissues

We analyzed primary samples obtained from consenting patients submitted to nephrectomy for renal cell carcinoma and preserved at San Raffaele URI Biobank (protocol URBBAN, IRB approval Sept. 2010). To perform a well-controlled analysis, we restricted the study to samples for which both OCT-embedded and frozen tissue pellet from cancer lesions were available. Furthermore, only those samples for which a non-cancerous tissue was also available as frozen pellet were included in the study.

METHOD DETAILS

Antibodies and Inhibitors

For western blot analysis we used antibodies against pP70S6K Thr389 (#9205 1:1000), pS6Rp Ser240/244 (#2215 1:5.000), S6RP (#2217 1:1000), TSC1 (#4906 1:1000), pAKT Thr308 (#9275 1:1000), pAKT Ser243 (#9271 1:1000), pERK Thr202/Tyr204 (#9101 1:1000), AKT (#9272 1:1000), ERK (#9102 1:1000) obtained from Cell Signaling Technology. P70S6K C-18 (#sc-230 1:1000), DAPI (# sc-3598 1:5000) Fh1 H-6 (sc393992 1:750) obtained from Santa Cruz Biotechnology. Vinculin V284 (#05-386 1:15.000) was obtained from Millipore. HIF1α (#10006421 1:250) was obtained from Cayman Chemical Company. For immunofluorescence staining LTL (Fluorescin Lotus Lectin) #FL-1321 and DBA (Rhodamine Dolichos Biflorus Agglutinin) #RL-1032 were obtained from Vector Laboratories and used 1:100. For immunohistochemistry we used antibodies against PAX2 ([EP3251] ab79389 1:1000), PAX8 ([PAX8R1] ab53490 5 μg/ml), Cytokeratin7 ([EPR17078] ab181598 1:8000), Nrf2 ([EP1808Y] ab62352, 1:150) from Abcam; Ki67 (RM-9106, 1:100) from Thermo Fisher; AMACR (NBP2-45491 1:150) from Novus Biologicals; pS6Rp Ser235/236 (#2211 1:5000) obtained from Cell Signaling Technology. Anti-5hmC (#V1339769, 1:1000) was obtained from Active Motif. Antibody against 2-SC residues were previously reported (Nagai et al., 2007).

HRP-conjugated secondary antibodies were from GE Healthcare, anti-rabbit HRP linked (#NA934V) and anti-mouse HRP linked (#NXA931). Rapamycin was obtained from LC Laboratories (#R-5000) dissolved in DMSO and used at a final concentration of 100nM for cell treatment. Mono-Methyl fumarate (MMF) was obtained from Sigma-Aldrich (#651419). For Rapamycin treatment MEF and IMCD cells were cultured sub-confluent in DMEM (GIBCO) supplied with 10% serum (Euroclone) and 1% Pen/Strep (GIBCO). Before treatment cells were serum starved overnight using DMEM supplied with 0.5% serum, 1% Pen/Strep. Cobalt chloride (#232696) was obtained from Sigma-Aldrich. For HIF1α stabilization, MEF cells were treated with 200nM Cobalt for 6 hr.

In vivo treatment

For MMF *in vivo* treatment, mice received daily (5 days per week) intra-peritoneal injections of 50mg/kg MMF solution (10%DMSO-90%NaCl) between P10-P30 (vehicle solution was used as treatment control). *T1*$^{f/+}$:Cre control littermates received either 1mg/kg MMF or vehicle alone. For Rapamycin (LC Laboratories, #R-5000) *in vivo* treatment, mice received daily intra-peritoneal injections of 1mg/kg Rapamycin solution (20%DMSO-80%NaCl) between P26-P30 (vehicle solution was used as treatment control). *T1*$^{f/+}$:Cre control littermate received either 1mg/kg Rapamycin or vehicle alone.

Histological analysis, immunofluorescence and immunohistochemistry

For histological analysis mice were sacrificed at the indicated time, kidneys were collected, weighted and fixed overnight in 4% Paraformaldehyde. Kidneys were subjected to a sucrose gradient (Sigma-Aldrich) from 10% to 30% in PBS, treated in 10% glycerol (Sigma-Aldrich), 30% sucrose in PBS and finally embedded in OCT (Bio Optica) for frozen sections.

For Hematoxylin-Eosin staining kidney sections were air-dried, rehydrated in PBS, incubated for 2 min and 30 s in 1:10 Harris Hematoxylin (Sigma-Aldrich), washed in water, incubated 5 min in Eosin G (Bio Optica), washed, processed through a dehydration alcohol scale and mounted in DPX (Sigma-Aldrich).

For immunofluorescence staining of DBA and LTL positive tubules 14μm kidney sections were washed in PBS, fixed 10 min in 4% Paraformaldehyde and permeabilized in 0.2% Triton X-100, PBS. We blocked sections in 5% Normal Goat serum (Sigma-Aldrich), 3%BSA, PBS for 1 hr at RT, incubated over night at 4°C with primary antibodies diluted in blocking solution, washed with PBS, the nucleus was stained with DAPI and mounted with moviol (Sigma-Aldrich). Images were obtained using UltraVIEW spinning disk confocal microscope (PerkinElmer) with a Plan Apochromat 63X/1.4 oil immersion or a 20X objective using the UltraVIEW ERS acquisition software.

For immunohistochemistry of PAX2, PAX8, CK-7, AMACR, NRF2, Ki67 and 5hmC kidneys were fixed in formalin 10% (Bio Optica), included in paraffin and cut 5 μm/slides. For 5hmC staining, the vendor instructions were followed.

For immunohistochemistry of pS6Rp on human ccRCC tissues, 10um sections were air-dried and washed in PBS. Endogenous peroxide was blocked for 10 min with 0.5% v.v. hydrogen peroxide in MetOH. Primary antibody was incubated O/N in 3%BSA,

5% NGS in PBS. The secondary antibody and the DAB$^+$ developing solution were from Dako (#K3468). Hematoxilin staining (2 min and 30 s) was used to visualize nuclei, sections were dehydrated and mounted in DPX (Sigma-Aldrich).

Cyst structures quantification analysis

To quantify the number of structures inside the cysts, we obtained longitudinal sections from the inner part of the kidney, performed Hematoxylin-Eosin staining and then obtained images with a 10x objective (Nikon Eclipse E600 microscope, Nikon Digital Camera DXM1200, ACT-1 software) for each kidney section. We used ImageJ program (http://rsb.info.nih.gov/ij/) to quantify the surface, expressed in pixels, covered by cysts in each kidney. We used a cutoff of 2000 pixels as the minimum surface that a cyst should have to be included in the analysis. We next counted all the cysts in the given section: 3 cortical and 3 medullary pictures from every kidney section (n = 3) of 3 different mutant mice and 3 relative controls. We next calculated the percentage of the different cysts with a given structure (cysts, cysts with papillae, cysts with cystadenomas, cysts with carcinomas) and normalized on total cyst number.

2SC and Ki67 IHC quantification: for the quantification of 2SC and Ki67 positive cells, n = 9 sections (n = 3 20x optical zoom fields for n = 3 section of the same kidney) were counted for n = 3 *T1$^{f/f}$:Cre* kidneys at P50 and P80.

5hmC IHC quantification: for the quantification of control tubules, nuclei from all the cells of 10 fields (20x optical zoom) for each sample (n = 3 controls) were counted. For the quantification of the three different lesions (cysts, papillae, and cystadenomas) 10 complete structures for each biological sample (n = 3 mutant P80 kidneys) were counted.

Metabolomic NMR analysis

Renal cortices samples were snap-frozen in liquid nitrogen and stored at −80°C until extraction. Snap-frozen samples were weighted before and after 24h lyophilization. Polar metabolites were extracted from the homogeneous dry tissue powder using a MeOH/$CHCl_3$ (1/1: v/v) solvent extraction strategy, as described in Lin et al. (2007). Polar phases were lyophilized for 24h, the resulting powder was then suspended in phosphate buffer 150 mM, containing 100 μM DSS as internal chemical shift reference and 0.02% sodium azide for sample preservation. Each sample had a final volume of 250 μL (H2O:D2O 90:10). NMR spectra were recorded at 298 K on a Bruker Avance 600 Ultra Shield TM Plus 600MHz spectrometer equipped with triple resonance cryoprobe (TCI), pulsed filed gradients and refrigerated autosampler (SampleJet). ^{1}H-1D NMR spectra (noesypr1d) were recorded with an acquisition time of 2 s, 128 transients and a relaxation delay of 6 s. ^{1}H-1D NMR spectra were typically processed with zero filling to 131k points, and apodized with an unshifted Gaussian and a 1 Hz line broadening exponential using Mnova 10.0 (Mestrelab Research).

Metabolites were identified and quantified using Chenomx 7.7 (Chenomx Inc., Edmonton, Canada), and Metabominer (Xia et al., 2008). For identification purposes 2D ^{1}H-^{1}H TOCSY and 2D ^{1}H-^{13}C HSQC spectra were also acquired on representative samples. 2D ^{1}H-^{1}H TOCSY spectra were acquired with a standard Bruker library pulse sequence (mlevphpr) with presaturation for water suppression, 2 s relaxation delay, 60ms mixing time, 36 transients and 512 increments. 2D ^{1}H-^{13}C HSQC spectra were acquired with a total of 90 transients for each of the 400 increments. Spectral widths were set to 12 and 170 ppm for ^{1}H and ^{13}C, respectively (off sets at 4.7 and 75 ppm, respectively). The water signal was eliminated using a presaturation continuous wave during the 3 s relaxation delay.

Post-processing of all the spectra was performed with Mnova 10.0 (Mestrelab Research), whereby DSS, water and urea peaks were excluded. After alignment, spectra were divided into regular buckets (0.04ppm). NMR data were then normalized to total area, Pareto scaled and subjected to principal component analysis (PCA) using MetaboAnalyst 3.0 (Xia et al., 2008). Partial least-squares-discriminant analysis (PLS-DA) was applied and variable importance in the projection (VIP) method was used to evaluate the significance of the bins in the separation. Bins with a variable importance in the projection (VIP) above 1 were considered important. This allowed to identify 50 and 51 bins that are responsible of the separation between Ctrls and mutants kidneys at P50 and P80, respectively. We were able to identify 32 (at P50) and 33 (at P80) metabolites from these bins. These were used for the KEGG-Pathways Based Overrepresentation Analysis shown in Figure 2C and 2D and listed in Table S1. Next, we performed a targeted analysis to determine the precise concentration of the individual metabolites in controls and mutant kidneys for direct comparison by univariate statistical analysis (Student's t test). The results are shown in Table S2.

LC-MS Metabolomic analysis

For metabolomic studies, mice were anesthetized and perfused in cold PBS before collecting kidneys. Collected kidneys were rapidly frozen at −80°C. Equal amounts of wet weight murine tissue were lysed in 250 μL extraction solution (30% acetonitrile, 50% methanol and 20% water) per 10 mg tissue in Bullet Blender (Next Advance), following the manufacturer's instructions. The suspension was immediately centrifuged (16,000*g*, 15 min at 0°C) and the supernatant used for LC–MS analysis. For the liquid chromatography separation, column A was Sequant Zic-Hilic (150 mm × 4.6 mm, 5 μm) with a guard column (20 mm × 2.1 mm, 5 μm) from HiChrom. Mobile phases. A: 0.1% formic acid (v/v) in water. B: 0.1% formic acid (v/v) in acetonitrile. Flow rate: 300 μL min^{-1}. Gradient: 0–3 min 80% B, 25 min 20% B, 26 min 80% B, 36 min 80% B. Column B was Seaquant Zic-pHilic (150 mm × 2.1 mm, 5 μm) with guard column (20 mm × 2.1 mm, 5 μm) from HiChrom. Mobile phases. C: 20 mM ammonium carbonate plus 0.1% ammonium hydroxide in water. D: acetonitrile. Flow rate: 100 μL min^{-1}. Gradient: 0 min 80% D, 28 min 20% D, 29 min 80% D, 45 min 80% D. The mass spectrometer (Thermo QExactive Orbitrap) was operated in full MS and polarity switching mode. Samples were randomized to avoid machine drifts. Spectra were analyzed using targeted approach. Spectra were analyzed using XCalibur Qual Browser and XCalibur Quan Browser softwares (Thermo Fischer Scientific) by referencing to an internal library of compounds. The arrays of spectra were then statistically analyzed using the functions explore.data and univariate of the R package muma (Gaude et al., 2013).

Statistical analysis of datasets followed established parameters for determination of significance and data distribution for metabolomics datasets (Gaude et al., 2013; Goodpaster et al., 2010). In brief, Shapiro–Wilk's test for normality was performed for every metabolite in each experimental condition. When the p value from Shapiro–Wilk's test was greater than 0.05, Welch's t test was performed, otherwise Wilcoxon–Mann–Whitney test was performed. p values were corrected for multiple testing using Benjamini–Hochberg correction. Metabolite abundance differences were considered significant when final corrected p value < 0.05.

For each different time point of analysis (P20, P50 and P80), t tests were used to identify metabolites that show statistical significant differential abundance between mutants and control, and p values have been corrected by using the Benjamini-Hochberg procedure (FDR-corrected t tests).

KEGG-Pathways Based Overrepresentation Analysis (ORA)

KEGG-Pathways Based Overrepresentation Analysis (ORA) has been developed to identify pathways that are significantly enriched in KEGG database starting from a list of metabolites. Such a list can be obtained using standard feature selection methods that statistically rank all the compounds and select those scoring above a certain threshold. Particularly, ORA applies the hypergeometric test to compute a statistical significance (p value) for each mouse pathways having at least one metabolite captured in the input list. Each p value has been corrected by using the Benjamini-Hochberg procedure and indicates the probability of seeing at least a particular number of metabolites from a certain pathways in the input list. In our analysis, in order to obtain the most significant pathways at the different disorder stages, we used as input the metabolites having FDR-corrected t tests < 0.01.

In vitro Fumarate quantification

Cells were plated the day before starting the assay in DMEM 10% FBS. Cells were treated with Rapamycin 100nm for 24 or 72 hr in DMEM 0.5% FBS ± Rapamycin (DMSO was used as control). Fumarate was measured using Fumarate Colorimetric Assay (BioVision #K633-100) according to manufacturer's instructions.

Estimation of Fumarate concentration

For the estimation in the concentration in the kidneys we calculated the fumarate concentration on the basis of tissue weight, considering the mM range given by NMR assay and the weight of the kidney (approximately 500mg for P80 *T1$^{f/f}$:Cre* kidneys) as previously performed for *Fh1*-mutant kidneys (Ternette et al., 2013). For the *in vitro* models, we calculated a concentration of 6 fmol/cell for *T1$^{-/-}$* MEFs and 4 fmol/cell for *T1$^{-/-}$* IMCDs. Assuming 10pL as the single cell volume this results in 0.6 and 0.4 mM respectively.

Soft-agar foci assay

For Soft agar foci assay, cells were first transfected with *Fh1-GFP* plasmid (Sciacovelli et al., 2016) or co-transfected with *Tsc1-Flag* (provided by Addgene and used in (Distefano et al., 2009) and pEGFP-NI plasmid (Clontech, #6085-1) using Lipofectamine 2000 as manufactured instructions (GFP plasmid was used as control). After one week, cells were collected and sorted. 10^4 positive cells were than plated in soft agar (0.5% GIBCO BactoAgar in DMEM 10% FBS), internal triplicates for each condition were used. Foci were counted three weeks after and divided according to diameter size. Wells were stained with Crystal Violet 0.05%, 20% methanol solution. For rapamycin and MMF treatment, cells were plated in soft agar (0.5% with 100nM Rapamycin or 100uM MMF).

Real-Time PCR analysis

Total RNA was isolated from plated cells using the RNAspin Mini kit (GE Healthcare, #25-0500-72). Total RNA from kidneys and human ccRCC nephrectomies was isolated using the NucleoZOL reagent (Macherey-Nagel, #740404.200) according to the manufacturer's instructions. cDNA was obtained by reverse transcription of extracted RNA using Oligo(dt)$_{15}$ primers (#C1101) and ImProm-II Reverse Transcriptase (#A3802) from Promega. Quantitative Real Time PCR analysis was performed on technical duplicates using SYBR Green I master mix (Roche, #04707516001) on LightCycler 480 Instrument (Roche). Primer sequences for qRT-PCR are reported in Table S3.

Western blot analysis

For western blot analysis cells or kidneys were lysed in lysis buffer solution of 150mM NaCl, 20mM Na_4HPO_4/NaH_2PO_4, 10% glycerol, 1% Triton X-100 (pH 7.2), complete protease inhibitor cocktail (Roche, #11836145001) and phosphatase inhibitors (1mM final concentration of glycerophosphate, sodium orthovanadate, and sodium fluoride). For Hif1α detection cells or kidneys were lysed in RIPA buffer solution (150mM NaCl, 50mM Tris-HCl pH 7.6, 1% NaDeoxycholate, 1% NP40, 0,1% SDS) complete protease and phosphatase inhibitors followed by three cycles of 5 min sonication. Total lysates were then quantified with Biorad Protein Assay (Biorad, #500-0006) and Laemmli buffer at a final concentration 2x was added to the samples. Proteins were next resolved in 4%–12% Tris-Glycine gradient gels (Life Technologies, #NP0335BOX) and then transferred onto polyvinylidene fluoride (PVDF) membranes (Millipore, #IPVH00010). We then blocked membranes with 5% milk in Tris-buffered saline, Tween 20 (TBS-T). All the primary antibodies for western blot analysis were diluted in 3% BSA (#A7906, Sigma-Aldrich), TBS-T. HRP-conjugated secondary antibodies were diluted 1:10.000 (or more if necessary) in 5% milk, TBS-T and detection was made with ECL (GE Amersham, #RPN2106) alone or supplied with 10% SuperSignal West Femto (Thermo Fisher Scientific, #34095) when necessary.

QUANTIFICATION AND STATISTICAL ANALYSIS

Student's t test, ANOVA, Shapiro–Wilk's test, Wilcoxon–Mann–Whitney test were used along the manuscript to test the statistical significances. p values were corrected for multiple testing by using Benjamini–Hochberg correction, Dunnett's test and Tukey's's test.

Prism 5, GraphPad Software, R and MATLAB® were used as statistical analysis tools, and p values are indicated in the legends.

DATA AND SOFTWARE AVAILABILITY

A MATLAB® implementation of KEGG-Pathways Based Overrepresentation Analysis is available upon request. The Mendeley doi for the full western blots from which the figures were cropped is https://doi.org/10.17632/vf53t5vb8h.1.